Evidence of the Ambipolar Behavior of Mo(6) Cluster Iodides in All-Inorganic Solar Cells: A New Example of Nanoarchitectonic Concept

Adèle Renaud, Pierre-Yves Jouan, Noée Dumait, Soraya Ababou-Girard, Nicolas Barreau, Tetsuo Uchikoshi, Fabien Grasset, Stéphane Jobic, Stéphane Cordier

Evidences of the Ambipolar Behaviour of Mo_6 cluster iodides in All Inorganic Solar Cells: A new example of Nanoachitechtonic concept

Adèle Renaud,[a] Pierre-Yves Jouan,[b] Noée Dumait,[a] Soraya Ababou-Girard,[c] Nicolas Barreau,[b] Tetsuo Uchikoshi,[c,e] Fabien Grasset,[a,d] Stéphane Jobic,[b] and Stéphane Cordier[a]*

[a]Univ Rennes, CNRS, ISCR – UMR 6226, F-35000 Rennes, France,

[b]Université de Nantes, CNRS, Institut des Matériaux Jean Rouxel, IMN, F-44000, Nantes, France

[c] Univ Rennes, CNRS, IPR – UMR 6251, F-35000 Rennes, France,

[d]CNRS–Saint-Gobain–NIMS, IRL 3629, Laboratory for Innovative Key Materials and Structures (LINK), National Institute for Materials Science, 1-1 Namiki, 305-0044 Tsukuba, Japan

[e]Research Center for Functional Materials, National Institute for Materials Science (NIMS), 1-1 Namiki, Tsukuba, Japan

KEYWORDS: Molybdenum octahedral cluster, ambipolar material, photoelectrochemistry, solar cell, electronic structure

ABSTRACT. Ambipolar materials such as carbon nanotubes, graphene or 2D transition metal chalcogenides are very attractive for a large range of applications; namely, light emitting transistors, logic circuits, gas sensors, flash memories, solar cells. In this work, it is shown that the nanoarchitectonics of inorganic Mo_6 cluster-based iodides enable to form thin films exhibiting photophysical properties that enable their classification as new members of the restricted family of ambipolar materials. Thus, electronic properties of the ternary iodide $Cs_2[\{Mo_6I^i_8\}I^a_6]$ and those of thin films of the aqua-complex-based compound $[\{Mo_6I^i_8\}I^a_4(H_2O)^a_2]\bullet xH_2O$ were investigated through an in-depth photoelectrochemical study. Once hole/electron pairs are created, the holes and electrons turn to be transported simultaneously in opposite directions and their lifetimes exhibit similar values. The ambipolar properties were demonstrated *via* the integration of

$[\{Mo_6I^i_8\}I^a_4(H_2O)^a_2]\bullet xH_2O$ as light-harvesters in an all solid solar cell. A significant photo-response with a typical diode characteristic clearly evidences the simultaneous transfer and transport of holes and electrons within the $[\{Mo_6I^i_8\}I^a_4(H_2O)^a_2]\bullet xH_2O$ layer. The ambipolar behavior results, on the one hand, from the confinement of electrons imposed by the nanometric size of the molecular metal clusters and, on the other hand, from poor electronic interactions between clusters in the solid state. The electronic structures of such molecular structure based layers are indeed comparable to those of intrinsic inorganic semiconductors.

1. INTRODUCTION.

Ambipolar materials are a class of semiconducting compounds that can intrinsically (i.e., without doping) transport and transfer simultaneously and equally both holes and electrons in comparable way.[1-3] Unlike conventional unipolar semiconductors where a type of charge carrier is predominant, ambipolar materials can display p-type and n-type characteristics within a single device, which makes them very attractive for many different application fields such as light emitting transistors,[3] logic circuits,[4] gas sensors,[5] flash memories,[6] solar cells,[7] etc. Only few materials such as semiconducting polymers,[6] carbon nanotubes,[8] 2D materials[4,9] or organic-inorganic hybrid perovskites[7] exhibit such an ambipolar behavior. The intriguing electronic properties of such compounds reside in their specific electronic structures which depend, on the one hand, on their chemical composition and crystalline nanostructures and, on the other hand, on

nanofeatures related to the size and morphology of the grains and/or crystallites that compose them. [1-3,10]

An important class of transition metal halides are those containing metal atom clusters (MC). The metal-metal bonds within the cluster is one of the intrinsic characteristic of MC. MC and halogen atoms form cluster units in the solid that can be viewed as perfect nano-objects. They contain a well-defined number of metal and halogen atoms and consequently they exhibit a well-defined nanometer size. This tri-dimensional size restriction brings to MC fascinating optical and electronic properties. This family of compounds exhibits an outstanding variety of structures and physical properties with a wide diversity of potential applications in various fields such as energy conversion and storage.[11-15]

In the chemistry of molybdenum halides, it is well known that Mo_6 molybdenum octahedral clusters are stabilized with 14 halogens to form $[\{Mo_6X^i_8\}X^a_6]$ units (i = inner position, a = apical position ; X = Cl, Br and I). Interestingly, various functional derivatives $[\{Mo_6X^i_8\}L^a_6]$ units where X^a is exchanged by a functional inorganic or organic group (L^a) are obtained combining solid-state chemistry and solution chemistry. On the structural point of view, the Mo_6 cluster is face-capped through covalent bonds to eight X^i ligands to form a $\{Mo_6X^i_8\}^{m+}$ cluster core that is coordinated with six additional L^a ligands. $[\{Mo_6X^i_8\}L^a_6]$ cluster units are the building blocks of a wide range of inorganic solid-state compounds, hybrid organic nanomaterials and supramolecular frameworks.[15-17] Depending on the charge of the apical ligands (i.e., neutral or negative), the cluster units can be charged positively, negatively or can even be neutral. In solids, the charge of MC units is compensated by inorganic or organic cations. The modulation of the number of electrons available for Mo−Mo bonding and the strength of electronic interactions between adjacent $[\{Mo_6X_8^i\}X_6^a]$ and $[\{Mo_6X_8^i\}L_6^a]$ units give rise to various properties.[15-17] For example,

nanosized molecular $[\{Mo_6X^i_8\}X^a_6]^{2-}$ MC units exhibit unique intrinsic optical and electronic properties such as molecule-like energy gaps, strong absorption in the visible and/or NIR spectral regions, deep red luminescence or high (photo)catalytic properties.[11-17]

These optoelectronic properties make them attractive materials for photovoltaic applications. Thus, $A_2[\{Mo_6Cl^i_8\}Cl^a_6]$ and $A_2[\{Mo_6Cl^i_8\}Cl^a_6]L_2$ series (with A = $N(C_4H_9)_4$ (tetrabutyl ammonium) or K and L = Cl, H_2O or CH_3CN (acetonitrile)) and $Cs_2[\{Mo_6I^i_8\}(CF_3CF_2COO)^a_6]$ were used as UV selective-harvesting luminophores for the design of transparent luminescent solar concentrators (TLSC)[13,18] and $Cs_2[\{Mo_6I^i_8\}I^a_6]$ (or more precisely $[\{Mo_6I^i_8\}I^a_4(H_2O)^a_2]$) was integrated as sensitizer in dye-sensitized solar cells (DSCs).[11,12] In this case, n- and p-type DSCs were prepared by the sensitization of TiO_2 and NiO electrodes by molybdenum cluster iodide, respectively (platinum was used as counter-electrode). Significant photocurrents were generated in both cells demonstrating unambiguously the amphoteric character of the $\{Mo_6I_8\}^{4+}$ cluster core. These charge transfers were made possible due to the appropriate alignment of energy levels between the n- and p-type semiconducting electrode work function and the frontier orbital energy levels (HOMO or LUMO) of the Mo_6-based compound. On the basis of all these convergent results, the ambipolar properties of the Mo_6 cluster iodides could be hypothesized.

Herein, we go a step further by evidencing this ambipolar character on the basis of (photo)-electrochemistry studies carried out both on the raw (as-prepared) metal cluster-based solid-state precursor based on $[\{Mo_6I^i_8\}I^a_6]^{2-}$ MC and on thin films resulting from the nanoarchitectonic[19] assemblies of $[\{Mo_6I^i_8\}I^a_4(H_2O)^a_2]$ building blocks to prepare photoelectrodes. As a demonstrator, an all inorganic solar cell integrating a layer of $[\{Mo_6I^i_8\}I^a_4(H_2O)^a_2]$ was designed. Remarkably, holes and electrons are injected from the MC layer to the p- and n-type semiconducting electrodes once the electron/hole pairs are generated.

2. EXPERIMENTAL SECTION

2.1. Materials and methods

$Cs_2[\{Mo_6I^i_8\}I^a_6]$ precursor synthesis. The chemicals were purchased from Sigma-Aldrich, VWR chemicals, Alfa Aesar and Acros, and were used as received. The $Cs_2[\{Mo_6I^i_8\}I^a_6]$ precursor powder was synthesized from MoI_2 and CsI solid-state chemistry at high temperature as previously described.[20]

Preparation of the Mo_6 cluster-based electrodes. Red transparent $[\{Mo_6I^i_8\}I^a_4(H_2O)^a_2].xH_2O$ photoelectrodes were prepared by electrophoretic deposition (EPD) process (Figure 1) from a Mo_6 cluster- based saturated solution consisting of the $Cs_2[\{Mo_6I^i_8\}I^a_6]$ precursor powder dissolved in acetone (HPLC grade, VWR Chemicals).[12] The EPD setup was composed of a clean fluorine tin oxide (FTO, SnO_2:F, Pilkington TEC8, 8 Ω/sq) substrate used as an anodic electrode and a stainless steel cathode, which were placed face-to-face with 1 cm between the two and connected to a Keithley Model 2450 Series SourceMeter with a carbon tape. The FTO substrates were previously cleaned in a three-step ultrasonication washing: first, in soapy water, second, in an acidified aqueous solution (few drops of hydrochloric acid, 37%, Sigma-Aldrich), and third in

ethanol. Finally, they were air-dried. Once the electrodes were immerged into the EPD solution, a continuous voltage (15 V) was applied for 30s. The applied voltage was stopped once the electrodes were out of the EPD solution and the solvent evaporated. The $Cs_2[\{Mo_6I^i_8\}I^a_6]$ precursor-based reference electrode was prepared from the precursor powder pressed under approximately 100 bars and dried during 1 hour in a vacuum chamber. The pellet was contacted in the backside with a copper wire using a carbon paste for a good electrical contact. This contact was then cured and sealed off with an epoxy resin (CaldoFix-2kit, Struers), and the pellet surface was polished (SiC paper, grid 1200 and 4000) to obtain a smooth electrode surface.

Solar cell fabrication. The MC-based all solid solar cell was prepared in a multiple step process. Firstly, the back layer consisting in a narrow metallic Ni° layer (resistivity in the range of μΩ.cm) was deposited by DC magnetron sputtering onto the glass substrate. Then, after to masque a part of the Ni film, a dense layer of NiO was deposited by reactive HiPIMS (High Power Impulse Magnetron Sputtering)[21] and was then recovered by the MC iodide layer (~300 nm thick) deposited by electrophoretic deposition (15 V for 30 s).[12] Third, the ZnO and ZnO:Al layers[22] (~ 300 nm thick) were then added by RF sputtering and a metallic Ni°-based grind was deposited to improve the electrical contact.

2.2 Characterization Techniques.

The X-ray powder diffraction (XRPD) patterns of the $Cs_2[\{Mo_6I^i_8\}I^a_6]$ precursor powder (denoted MC precursor) and that of the $[\{Mo_6I^i_8\}I^a_4(H_2O)^a_2]\bullet xH_2O$ film (denoted MC film) were collected at room temperature in a 2θ angle ranging from 5 to 90 ˚ with a scan speed of 4 ˚·min-1 with a Bruker D8 Advance two-circle diffractometer (θ-2θ Bragg–Brentano mode) using Cu Kα radiation (l = 1.54056 Å) equipped with a Ge(111) monochromator and a Lynx Eye detector (Figure 2c). The grazing incidence X-ray diffraction patterns (GIXRD) were obtained on a thin film of $[\{Mo_6I^i_8\}I^a_4(H_2O)^a_2].xH_2O$ by using a diffractometer (SmartLab, Rigaku Corp., Tokyo, Japan) equipped with a copper Kα radiation (λ = 1.5406 Å) at 50 mA and 40 kV power (Figure S1). The incident beam was set at fixed critical w angles ($0.2^\circ \leq w \leq 0.8^\circ$). The UV-vis transmission spectrum of the transparent $[\{Mo_6I^i_8\}I^a_4(H_2O)^a_2]\bullet xH_2O$ based photoelectrodes were obtained on a V-770 JASCO spectrophotometer and the $Cs_2[\{Mo_6I^i_8\}I^a_6]$ precursor powder reflectance spectrum was obtained on the same spectrophotometer using the integrated reflectance sphere accessory (Figure 3). The MC precursor powder and film surface were analyzed by X-ray photoelectron spectroscopy (XPS) technique (Figures 2b, S2, S3 and S4). Measurements were performed with an Mg Kalpha (hν) 1254 eV X-ray source, using a VSW HA100 photoelectron spectrometer with

a hemispherical photoelectron analyzer, working at an energy pass of 20 eV for survey and resolved spectra. The experimental resolution was 1.0 eV. Binding energies were referenced to the C1s signal fixed at 285,0 eV. Data were treated after a Shirley background subtraction using a mixed of Gaussian- Lorentzian product. Raman scattering spectra of $Cs_2[\{Mo_6I^i_8\}I^a_6]$ powder and that of the thin films of $[\{Mo_6I^i_8\}I^a_4(H_2O)^a_2]\bullet xH_2O$ were recorded using a LabRam High Resolution spectrometer coupled with a confocal microscope (Horiba Jobin Yvon), 600 g mm^{-1} and 100 × objective. A laser diode 785 nm was used for scattering excitation. Raman spectra were recorded at room temperature with 5 s exposition and 2 accumulations for the $Cs_2[\{Mo_6I^i_8\}I^a_6]$ powder and 30 s exposition and 2 accumulations. Spectra were recorded at different points of accumulation in order to check the homogeneity of powder and films. The electrochemical measurements (Figure 4 and 5) were carried out using a three-electrode set-up, namely the MC-based electrode as working electrode, a Pt wire as counter-electrode and a reference in Ag/AgCl, all dipped in a KCl (0.5 M in aqueous media) electrolyte. Steady state and transient (photo)-electrochemical measurements were recorded using an Autolab PGSTAT204 (Metrohm AG) equipped with a FRA32M electrochemical impedance spectroscopy module. The photoelectrochemical measurements were recorded under an MI-LED illuminator (Edmund

Optics). The impedance spectra were measured in a frequency range from 100 Hz to 100 kHz. The Mott–Schottky analyses were recorded in a potential range of -0.5 to 0.5 vs Ag/AgCl at relatively high frequencies (1–10 kHz) allowing to neglect the diffusion phenomena. Thus, the interface semiconductor/electrolyte capacitance (C) was determined using a simplified Randles equivalent circuit by neglecting the Warburg component at high frequency. The C values for an applied potential were calculated from the constant phase element (CPE, $Z_{CPE} = 1/Q(j\omega)^{\alpha}$, where $0 < \alpha < 1$) reflecting the nonideality of the interface capacitance using $C = (1/R_s + 1/R_{tc})^{(\alpha-1)/\alpha}Q^{1/\alpha}$. Flat band potentials ($V_{fb}$) were determined by extrapolation at $C^{-2} = 0$ from the Mott-Schottky plot (C_{SC}^{-2} vs V), which utilizes the Mott−Schottky equation for a n-type semiconductor (Equation 1) and Fermi levels were approximated (E_{fb} (eV) = - 4.5 – e.V_{fb} (RHE)[23]).

$$\frac{1}{C_{SC}^2} = \frac{2}{\varepsilon\varepsilon_0 e A^2 N}\left(V - V_{fb} - \frac{kT}{e}\right) \qquad \text{(Equation 1)}$$

C_{SC} corresponds to the capacitance in the space charge region of the semiconductor, A the interfacial surface area between the semiconductor electrode and electrolyte, k the Boltzmann constant, T the temperature, e the electron charge, ε_0 the vacuum permittivity, and ε the relative permittivity of the semiconductor. C_{SC}^{-2} was approximated to be C^{-2} due to the large capacitance of the Helmholtz layer, at the semiconductor surface in the electrolyte, in comparison to C_{SC}. Scanning microscopy image (Figure 5a) was collected on a JEOL JSM 7100 F microscope

operating at 10 kV. The solar cell performances were recorded on a Keithley model 2420 digital source meter under AM1.5G simulated sunlight (1000 $W \cdot m^{-2}$).

3. RESULTS AND DISCUSSION

Transparent $[\{Mo_6I^i_8\}I^a_4(H_2O)^a_2].xH_2O$-based photoelectrodes were obtained by electrophoretic deposition of Mo_6 clusters onto fluorine tin oxide (FTO) substrates (Figure 1).[12]

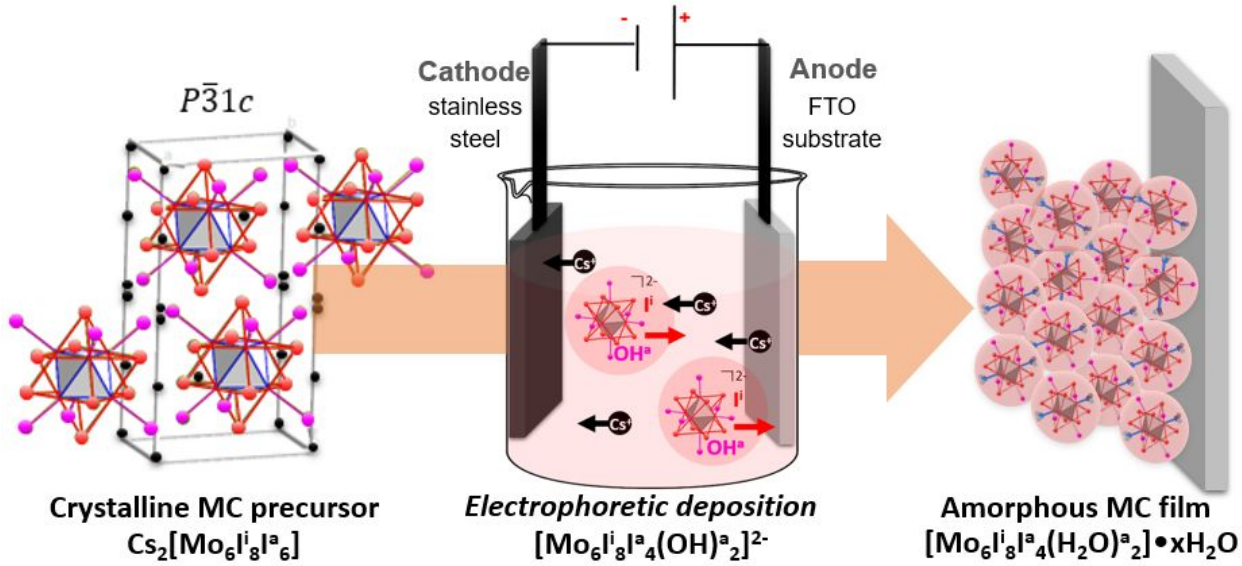

Figure 1. Methodology of preparation of amorphous MC films by electrophoretic deposition from the crystalline MC precursor dissolved in acetone.

The MC films obtained of ~800 nm thick (Figure 2a) are amorphous (see TEM image in insert of Figure 2a and XRD diagrams in Figure 2c and S1 (grazing incidence X-ray)) and have a

composition slightly different of the precursor powder (Figure 1). Indeed, according to our previously described methodology,[12] the crystalline $Cs_2[\{Mo_6I^i_8\}I^a_6]$ precursor was dissolved in acetone to form Cs^+ and $[\{Mo_6I^i_8\}I^a_6(OH)^a_{2-x}(solvent)^a_x]^{n-}$ ions, or more probably $[Mo_6I^i_8I^a_4(OH)^a_2]^{2-}$ anion, which generates $[\{Mo_6I^i_8\}I^a_4(H_2O)^a_2].xH_2O$ when neutralized by H_3O^+ at the substrate surface.[12,24-26] The conservation of the $\{Mo_6I^i_8\}$ metallic cluster core was demonstrated by XPS and Raman spectroscopy analyses. Indeed, XPS analyses proved that the Mo 3d ($Mo3d_{3/2}$ and $Mo3d_{3/2}$, Figure S3b) contributions recorded on MC precursor powder and film are exactly similar. Moreover, the 99, 113, 133 and 158 cm^{-1} bands obtained by Raman spectroscopy for the MC film can be assigned respectively to the Mo-Mo (94 and 108 cm^{-1} for the MC precursor powder), Mo-I^i (130 and 154 cm^{-1} for the MC precursor powder) and Mo-I^a (113 cm^{-1} for the MC precursor powder) vibration modes.[27] The enlargement of the bands is attributed to the loss of symmetry due to the substitution of a part of the iodine apical ligand by water. The substitution of two I^a is clearly highlighted by X-ray spectroscopy (EDS) analyses (I/Mo ratio equals to 12/6 and 14/6 for the film and the powder respectively) and XPS characterizations. Indeed, by comparing XPS spectra of the MC film and precursor powder (Figure 2b and S3a), the apical contributions of the I 3d peaks ($3d_{5/2}$ and $3d_{3/2}$) decrease after the deposition of Mo_6 clusters and tend to a I^i/I^a ratio of 2 (compared to 4/3 in theory).[28] This is concomitant with the decrease of the Cs content. Indeed, Cs was not detected in MC films by EDS and was characterized only on the first atomic layers by XPS. The Cs contribution ($3d_{5/2}$ peak, Figure S4) decreases of 90% compared to MC precursor powder whereas the Mo 3p and 3d peaks are not modified.

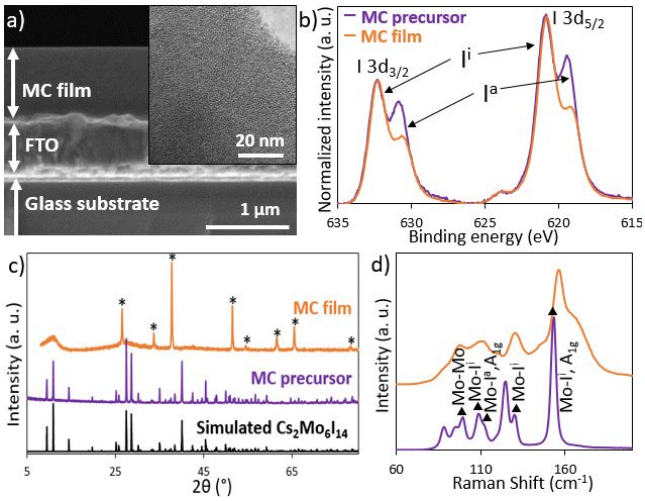

Figure 2. a) SEM and TEM (insert) images of the MC film. b) XPS, c) XRD and d) RAMAN characterizations of a MC film compared to the MC precursor powder. XRD patterns were compared to the simulated diagram of $Cs_2[\{Mo_6I^i_8\}I^a_6]$.[20] Stars in c) correspond to the FTO substrate (tetragonal SnO_2 phase, space group *P42/mnm*) and triangles in d) correspond to bands assigned to $[Mo_6I_{14}]^{2-}$ vibration modes.[27]

Thus, Raman and XPS analyses of the films agree with the general formulation $[\{M_6X_8\}X'_4(H_2O)_2]$ (M = W, Mo ; X = Cl, Br and I, X' = Cl, Br and I) reported by H. Baumann et al.[30] and H. Schäfer *et al.*[26] Several compounds based on this $[\{M_6X_8\}X'_4(H_2O)_2$ general formula are reported by these authors. They all crystallize with the $[\{M_6Br_8\}Br_4(H_2O)_2]$ structure type (tetragonal, space group *I*4/*m*) reported by L. J. Guggenbekger *et al.*[25] More recently, the structural investigations of several aqua hydroxo complexes based on $\{Mo_6I_8\}^{4+}$ cluster core have been reported namely $[\{Mo_6I_8\}(H_2O)_4(OH)_2](An)_2.nH_2O$ (An = NO_3^-, n = 3; An = OTs^-, n = 2, OTs^--p-toluenesulfonate)][31] and $[\{Mo_6I_8\}(OH)_4(H_2O)_2].nH_2O$ (n = 2, 12, 14).[32] It turns out that after substitution of apical ligands by water molecules or hydroxo groups, the $[\{Mo_6I_8\}(OH)_4(H_2O)_2]$ cluster units crystallize along with water molecules. The X-ray diffraction

analyses of the thin films obtained in the title work indicate an amorphous structuration meaning no long range ordering of the $[\{Mo_6I_8\}I_4(H_2O)_2]$ cluster units. Following the assumption that the formation of $[\{Mo_6I_8\}I_4(H_2O)_2]$ corresponds to the neutralization, close the surface, of $[\{Mo_6I_8\}I_4(OH)_2]^{2-}$ by 2 H_3O^+, it is understandable that the thin films also contains water molecules. The composition of the thin films should correspond to $[\{Mo_6I_8\}I_4(H_2O)_2]$ along with 2 water molecules at least. Hence the chemical composition of thin films is denoted $[\{Mo_6I^i_8\}I^a_4(H_2O)^a_2]$.$xH_2O$ all along the manuscript.

Despite the composition modification, it is worth noting that the $[\{Mo_6I^i_8\}I^a_4(H_2O)^a_2]$.$xH_2O$-based films (MC films) and the $Cs_2[\{Mo_6I^i_8\}I^a_6]$ precursor (MC precursor) both exhibit strong absorption properties in the visible region with a similar optical bandgap of 1.9 eV (Figure 3).

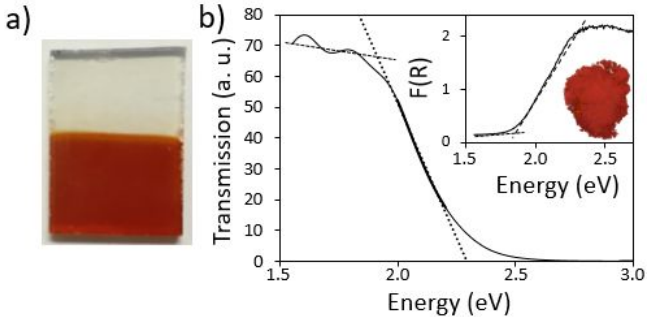

Figure 3. a) Photograph of a MC iodide-based photoelectrode and b) UV-vis transmission spectrum. The insert corresponds to the photograph and the Kubelka-Munk transform of the $Cs_2[\{Mo_6I^i_8\}I^a_6]$ powdered precursor.

Electronic properties of the MC films were characterized once integrated in the electrochemical cell. Steady state and transient (photo)-electrochemical measurements are gathered in Figure 4 and

5. Chronopotentiometry, current-potential and impedance curves under chopped or constant illumination highlight the photo-response of the MC-based photoelectrodes. Nyquist diagrams recorded under light and in the dark at open circuit potential (OCP) were modeled by a classical Randles equivalent circuit (see Figure 5a). The significant decrease of the semicircle under the light translates an increase of charge transfer rate between the photoelectrode and the electrolyte. The charge-transfer conductivity calculated from R_{tc} was found to be 4-fold enhanced when the photoelectrode is illuminated (9.10^{-8} and 4.10^{-7} $S.cm^{-1}$ in the dark and under the light, respectively). This enhancement results in the great improvement of the current generated under the light as observed in Figure 4a. This current-potential curve measured under chopped illumination clearly highlights the ambivalent behavior of such MC-based photoelectrodes. Indeed, for low potentials a photo-reduction current is observed when the electrochemical cell is illuminated whereas a photo-oxidation current is measured when the applied potential becomes higher than the reversal potential. This frontier potential corresponding to the photocurrent onset potential is located around 0.36 V vs Ag/AgCl. This photocurrent inversion translates the inversion of the charge carrier type at the photoelectrode surface. For an inorganic unipolar semiconductor in depletion condition, the photocurrent indicates the minority charge carrier type, namely holes and electrons

for photo-reduction and photo-oxidation, respectively. The inversion of photocurrent is caused by the inversion of the band bending at the semiconductor surface. Commonly, in accumulation situation, the photocurrent values are very low compared to those in depletion conditions. This is not the case here for the molecular MC-based photoelectrodes where the photo-oxidation and photo-reduction current values are comparable and evolve symmetrically on either side of the reversal potential. Consequently, this result indicates comparable electron and hole transport characteristics and strongly suggests ambipolar properties for the $[\{Mo_6I^i_8\}I^a_4(H_2O)^a_2]\cdot xH_2O$ material.

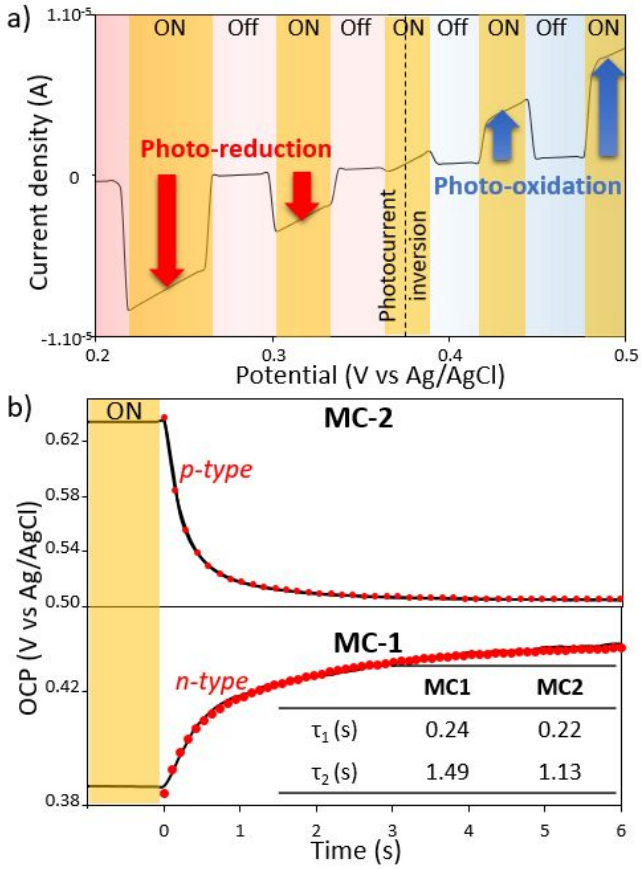

Figure 4. Steady state photoelectrochemical measurements. a) Current-potential curve measured under chopped illumination on a $[\{Mo_6I^i_8\}I^a_4(H_2O)^a_2]$•xH2O film. The yellow regions corresponds to the illuminated periods. b) Open circuit potential (OCP) decay of two MC-based photoelectrodes (n-type and p-type) after stopping the illumination and charge carrier lifetime determined by fitting of the curves by exponentials.

In order to further investigate the charge transport properties in the MC layer, the photopotential at equilibrium was studied. The evolution of the open circuit potential (OCP) appears very dependent of the potential in the dark and, very likely, to the surface state. For two Mo_6 cluster iodide-based films prepared in the same conditions (MC-1 and MC-2 in the Figure 4b), we can

observe the two possible exponential decay behaviors of the OCP under illumination, namely an OCP decrease (p-type behavior) or an OCP increase (n-type behavior). This suggests once more, the ambipolar behavior of the MC material. One can assume that this particular behavior is due to close values of the photoelectrode/electrolyte equilibrium potentials (OCP) and the photocurrent onset potential. When the OCP is slightly higher (lower) than the photocurrent onset potential, an n-type (p-type) behavior is observed.

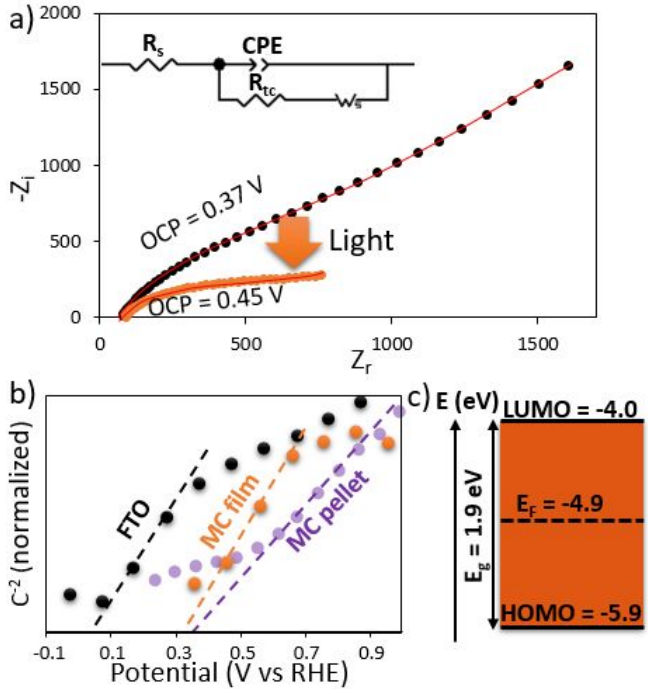

Figure 5. Transient (photo)-electrochemical measurements. a) Nyquist diagrams of electrochemical circuit in dark and under illumination at open circuit potential and the equivalent circuit used to fit them. b) Mott-Schottky plots for the MC film deposited on FTO, the FTO substrate and the $Cs_2[\{Mo_6I^i_8\}I^a_6]$ dense pellet depicted versus RHE by using the formulae $V_{fb}(RHE) = V_{fb}(Ag/AgCl) + 0.059\ pH + VAg/AgCl(RHE)$[23] c) Energy levels (absolute scale with

respect to vacuum level) of MC iodide layer determined by coupling optical and electrochemical measurements.

Electrochemical impedance spectroscopy measurements were carried out to access to the majority charge carriers and the flat band potential. Mott-Schottky plot for MC film is depicted versus the RHE (reversible hydrogen electrode) in Figure 5b and is compared to those obtained for FTO substrate and $Cs_2[\{Mo_6I^i_8\}I^a_6]$ precursor-based dense pellet. A straight line with a positive slope characteristic of n-typeness is observed for all electrodes that finally indicates that the transport in the MC compound is dominated by electron transport. Let us point out that the electron lifetime determined by fitting the OCP decay (OCPD) is although slightly higher than the hole lifetime in the same order of magnitude (Figure 4b and S5). This is consistent with the ambipolar behavior of MC films. A flatband potential of 0.35 V vs RHE corresponding to a Fermi level of -4.9 eV (on an absolute energy scale with respect to the vacuum level) was found. The energy level diagram (Figure 5c) of MC film was built from flat band potential, bandgap and electrochemistry (HOMO-LUMO) investigations.[11] It appears that the measured Fermi level pins exactly at the middle of the bandgap as for an intrinsic semiconductor. Such behavior has already been measured and reported for monolayers of $[\{Mo_6Br^i_8\}(NCS)^a_2]^{2-}$ deposited on gold surfaces.[33] This probably

originates from the confinement of electrons within the nanosized metallic molecular clusters. Indeed as reported for the $Cs_2[\{Mo_6X^i_8\}X^a_6]$ series (X = Cl, Br and I)[29] and in particular for $Cs_2[\{Mo_6I^i_8\}I^a_6]$, the electronic states of every cluster within the solid are highly localized. Every band possesses a small dispersion in *k*-space. The electronic structure of $[\{Mo_6X^i_8\}X^a_6]$ based solid state compounds strongly derives from the molecular orbital diagram of discrete $[\{Mo_6X^i_8\}X^a_6]^{2-}$ cluster units characterized by discrete energy levels. A similar situation is expected for thin films of $[\{Mo_6I^i_8\}I^a_4(H_2O)^a_2].xH_2O$. The molecular orbital diagram of $[\{Mo_6I^i_8\}I^a_4(H_2O)^a_2]$ cluster's building blocks is not disturbed by staking effects including the insertion of water molecules once deposited on surfaces. Electronic structures of molecular cluster-based layers could thus be related to that of intrinsic inorganic semiconductors with a localization of the Fermi level at the middle of the band gap. These features should be at the origin of the ambivalent behavior of these materials.

In order to definitely demonstrate the ambipolar properties of MC iodide, and highlight its capacity to transfer simultaneously electron and hole, a first all solid solar cell was set up. It consists of a MC layer sandwiched between two charge extractors, i.e., a NiO/Ni° hole extractor electrode and a ZnO/ZnO:Al electron one (Figure 6). First, in order to improve the electrical

contact, a narrow metallic Ni° layer (resistivity in the range of μΩ.cm) was deposited by DC magnetron sputtering onto the glass substrate. Then, we have masque a part of this film (back electrode) and we proceed of the deposition of the other coatings. First NiO dense layer (under 50 nm, resistivity in the range of 50 Ω.cm) was deposited by reactive HiPIMS (High Power Impulse Magnetron Sputtering)[21] and was secondly recovered by the MC iodide layer (~300 nm thick) deposited by electrophoretic deposition.[12] Third, the ZnO and ZnO:Al layers[22] (~ 300 nm thick) were then added by RF sputtering and a metallic Ni°-based grind was deposited to improve the electrical contact. A photograph of the solar cell is depicted in the insert of Figure 5a. The red color is deemed to represent the color of the MC iodide absorber.

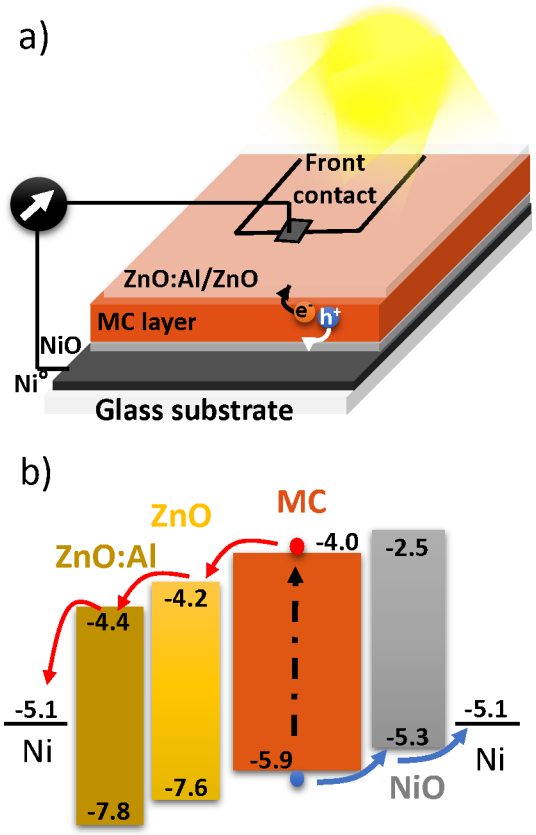

Figure 6. Schematic representation of a) MC-based all solid solar cell and b) energy levels of each layer on an absolute scale with respect to vacuum.

Figure 7b depicts the current–voltage characteristics in the dark and under AM1.5 illumination (1000 $W.m^{-2}$) of this p-i-n junction. A significant photo-response with a diode characteristic is clearly observed. This demonstrates unambiguously the simultaneous hole and electron injection from the MC layer to the p- and n-type semiconducting electrodes, respectively and thereby the ambipolar behavior of Mo_6 cluster iodide. These charge carrier transports are possible across the solar cell because of the full adequacy between the energy levels of each layer (see Figure 6b).

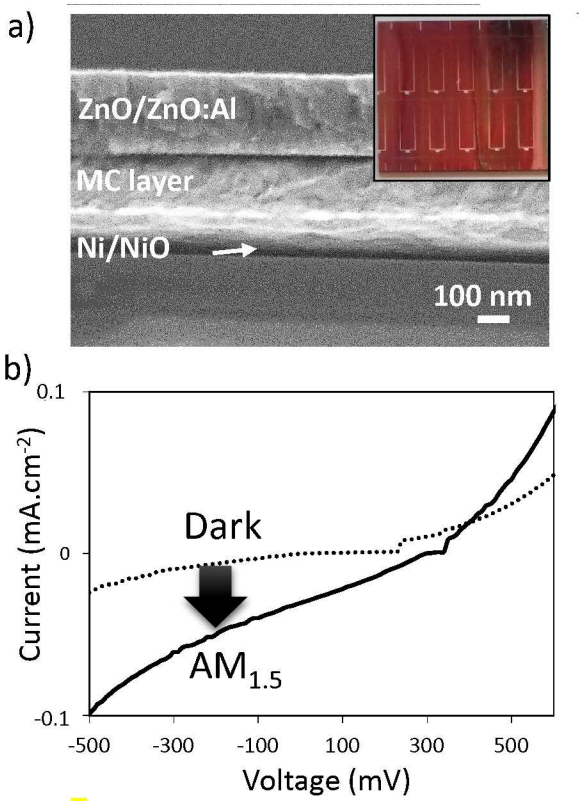

Figure 7. Schematic representation of a) MC-based all solid solar cell and b) I(V) measurements in the dark and under AM1.5 illumination.

4. CONCLUSIONS

In conclusion, molybdenum cluster iodides appears as new members of the inorganic ambipolar materials family like carbon nanotube, graphene and transition metal chalcogenides. The ambipolar properties were highlighted on the raw solid-state precursor based on $[\{Mo_6I^i_8\}I^a_6]^{2-}$ MC units, namely $Cs_2[\{Mo_6I^i_8\}I^a_6]$, and once integrated as $[\{Mo_6I^i_8\}I^a_4(H_2O)^a_2]$ building blocks by EPD technic in photoelectrodes. A demonstrator integrating a layer of $[\{Mo_6I^i_8\}I^a_4(H_2O)^a_2]$ as solar light harvester was designed. The holes and electrons photogenerated within the MC layer

turn to be transported simultaneously in opposite directions and their lifetimes exhibit similar values. Holes and electrons are injected from the MC layer to a NiO/Ni° hole extractor electrode and to a ZnO/ZnO:Al electron one. These outstanding electronic behaviors results from the confinement of electrons within the nanosized metallic molecular clusters. The molecular structure of the cluster's building blocks is not disturbed by solid-state staking effects or once deposited on surfaces. Electronic structures of molecular cluster based compounds and layers are thus related to that of intrinsic inorganic semiconductors. MC clusters are known to be very versatile materials. Their properties can be efficiently improved by combining solid-state chemistry and solution chemistry giving rise to a wide range of hybrid materials and functional surfaces with tunable optical properties.[16,17] Remarkably, it has been demonstrated in this work that they belong also to the restricted of ambipolar materials. The nanoarchitectonic applied to molecular clusters opens the way to new outlooks and potential applications in the field of photovoltaics for the collection of light and the generation of electron/hole pairs or in the field of electroluminescent transistors for their excitonic recombination capacities.

ASSOCIATED CONTENT

Supporting Information. The supporting information is available free of charge. Grazing incidence X-ray diffraction patterns (GIXRD) of the $[\{Mo_6I^i_8\}I^a_4(H_2O)^a_2].xH_2O$ photoelectrode, XPS analyses (wide-range spectra, I 3d, Mo 3d and Cs 4d) obtained on the MC film and the MC precursor powder and charge carrier lifetimes determined on the MC film *via* the OCP decay (file type, i.e., PDF).

AUTHOR INFORMATION

Corresponding Author

*Dr. Adèle Renaud, Univ Rennes, CNRS, ISCR – UMR 6226, F-35000 Rennes, France, adele.renaud@univ-rennes1.fr

Author Contributions

The manuscript was written through contributions of all authors. All authors have given approval to the final version of the manuscript.

Notes

The authors declare no competing financial interest.

ACKNOWLEDGMENT

The authors thank CMEBA plateform (Francis Gouttefangeas and Loic Joanny) from UMS 2001 ScanMAT CNRS-Université Rennes 1 for the FE-SEM images and analyses. Grazing incidence X-ray diffraction (GIXRD) and Raman investigations were performed using facilities available on respectively OSIRIX and SIR Plateforms from UMS 2001 CNRS-Université Rennes 1. The authors are very grateful to Bertrand Lefeuvre ISCR UMR 6226 CNRS- Université Rennes and Grégory Taupier from UMS 2001 CNRS-Université Rennes 1 and Alain Moréac from IPR UMR 6252 CNRS-Université Rennes1.

REFERENCES

(1) Ren, Y.; Han, S.-T.; Zhou, Y. *CHAPTER 1: Introduction and Fundamental Principles of Ambipolar Materials*, Ambipolar Materials and Devices, RSC, 2021; pp 1-13. DOI: 10.1039/9781788019279-00001

(2) Ren, Y.; Yang, X.; Zhou, L.; Mao, J.-Y.; Han, S.-T.; Zhou, Y. Recent Advances in Ambipolar Transistors for Functional Applications, *Adv. Funct. Mater.* **2019,** *29*, 1902105.

(3) Bisri, S. Z.; Piliego, C.; Gao, J.; Loi, M. A. Outlook and Emerging Semiconducting Materials for Ambipolar Transistors, *Adv. Mater.* **2014**, *26*, 1176-1199.

(4) Lin, Y.-F.; Xu, Y.; Wang, S.-T.; Li, S.-L.; Yamamoto, M.; Aparecido-Ferreira, A.; Li, W.; Sun, H.; Nakaharai, S.; Jian, W.-B.; Ueno, K.; Tsukagoshi, K.; Ambipolar $MoTe_2$ Transistors and Their Applications in Logic Circuits, *Adv. Mater.* **2014**, *26*, 3263-3269.

(5) Wannebroucq, A.; Ouedraogo, S.; Meunier-Prest, R.; Suisse, J.-M.; Bayo, M.; Bouve, M.; On The Interest of Ambipolar Materials for Gas Sensing, *Sens. Actuat. B Chem.* **2018**, *258*, 657-664.

(6) Zhou, Y.; Han, S.-T.; Sonar, P.; Roy, V. A. L.; Nonvolatile Multilevel Data Storage Memory Device from Controlled Ambipolar Charge Trapping Mechanism, *Sci. Rep.* **2013**, *3*, 2319.

(7) Giorgi, G.; Yamashita, K.; Organic–Inorganic Halide Perovskites: An Ambipolar Class of Materials with Enhanced Photovoltaic Performances, *J. Mater. Chem. A* 2015, *3*, 8981-8991.

(8) Kim, B.; Geier, M. L.; Hersam, M. C.; Dodabalapur, A.; Inkjet Printed Circuits Based on Ambipolar and P-type Carbon Nanotube Thin-Film Transistors, *Sci. Rep.* 2017, *7*, 39627.

(9) Myung, S.; Park, J.; Lee, H.; Kim, K. S.; Hong, S. Ambipolar Memory Devices Based on Reduced Graphene Oxide and Nanoparticles, *Adv. Mater.* 2010, *22*, 2045-2049.

(10) Natali, D. ; Caironi, M.; Charge Injection in Solution-Processed Organic Field-Effect Transistors: Physics, Models and Characterization Methods, *Adv. Mater.* 2012, *24*, 1357-1387.

(11) Renaud, A.; Grasset, F.; Dierre, B.; Uchikoshi, T.; Ohashi, N.; Takei, T.; Planchat, A.; Cario, L.; Jobic, S.; Odobel, F.; Cordier, S. Inorganic Molybdenum Clusters as Light-Harvester in All Inorganic Solar Cells: A Proof of Concept, *ChemistrySelect.* 2016, *1*, 2284-2289.

(12) Renaud, A.; Nguyen, T. K. N.; Grasset, F.; Raissi, M.; Guillon, V.; Delabrouille, F.; Dumait, N.; Jouan, P.-Y.; Cario, L.; Jobic, S.; Odobel, F. ; Cordier, S.; Uchikoshi, T.; Preparation by electrophoretic deposition of molybdenum iodide cluster-based functional nanostructured photoelectrodes for solar, cells, *Electrochimica Acta* 2019, *317*, 737-745.

(13) Zhao, Y.; Lunt, R. R. Transparent Luminescent Solar Concentrators for Large-Area Solar Windows Enabled by Massive Stokes-Shift Nanocluster Phosphors, *Adv. Energy Mater.* 2013, *3*, 1143-1148.

(14) Feliz, M.; Puche, M.; Atienzar, P.; Concepción, P.; Cordier, S.; Molard, Y.; In Situ Generation of Active Molybdenum Octahedral Clusters for Photocatalytic Hydrogen Production from Water, *ChemSusChem* **2016**, *9*, 1963-1971.

(15) Dierre, B.; Costuas, K.; Dumait, N.; Paofai, S.; Amela-Cortes, M.; Molard, Y.; Grasset, F.; Cho, T.; Takahashi, K.; Ohashi, N.; Uchikoshi, T.; Cordier, S. ; Mo_6 Cluster-Based Compounds for Energy Conversion Applications: Comparative Study of Photoluminescence and Cathodoluminescence, *Sci. Technol. Adv. Mater.* **2017**, *18*, 458-466.

(16) Prabusankar, G.; Molard, Y.; Cordier, S.; Golhen, S.; Le Gal, Y.; Perrin, C.; Ouahab, L.; Kahlal, S.; Halet, J.-F.; Experimental and Theoretical Evidence of π-d Interactions in Supramolecular Assemblies Based on TTF-CH=CH-Py Ligands Tethered to $Mo_6X^i_8$ Octahedral Molybdenum Halide Cluster Cores, *Eur. J. Inorg. Chem.* **2009**, *2009*, 2153-2161.

(17) Cordier, S.; Grasset, F.; Molard, Y.; Amela-Cortes, M.; Boukherroub, R.; Ravaine, S.; Mortier, M.; Ohashi, N.; Saito, N.; Haneda, H. Inorganic Molybdenum Octahedral Nanosized Cluster Units, Versatile Functional Building Block for Nanoarchitectonics, *J. Inorg. Organomet. Polym. Mater.* **2015**, *25*, 189-204.

(18) Yang, C.; Sheng, W.; Moemeni, M.; Bates, M.; Herrera, C. K.; Borhan, B.; Lunt, R. R.; Ultraviolet and Near-Infrared Dual-Band Selective-Harvesting Transparent Luminescent Solar Concentrators, *Adv. Energy Mater.* **2021**, *11*, 2003581.

(19) Ariga, K; Nanoarchitectonics: What's Coming Next After Nanotechnology?, *Nanoscale Horiz.* 2021, 6, 364-378.

(20) Kirakci, K.; Cordier, S.; Perrin, C.; Synthesis and Characterization of $Cs_2Mo_6X_{14}$ (X = Br or I) Hexamolybdenum Cluster Halides: Efficient Mo_6 Cluster Precursors for Solution Chemistry Syntheses, *Z. Anorg. Allg. Chem.* **2005**, *631*, 411.

(21) Keraudy, J.; Delfour-Peyrethon, B.; Ferrec, A.; Garcia Molleja, J.; Richard-Plouet, M.; Payen, C.; Hamon, J.; Corraze, B.; Goullet, A.; Jouan, P.-Y.; Process- and Optoelectronic-Control of NiOx Thin Films Deposited by Reactive High Power Impulse Magnetron Sputtering, *J. Appl. Phys.* **2017**, *121*, 171916.

(22) Shi, W.; Theelen, M.; Illiberi, A.; Barreau, N.; van der Sar, S. J.; Butterling, M.; Schut, H.; Egger, W.; Dickmann, M.; Hugenschmidt, C.; Zeman, M.; Brück, E.; Eijt, S. W. H. Evolution and Role of Vacancy Clusters at Grain Boundaries of ZnO:Al During Accelerated Degradation

of Cu(In,Ga)Se_2 Solar Cells Revealed by Positron Annihilation, *Phys. Rev. Mater.* **2018**, *2*, 105403.

(23) Bais, P.; Caldes, M.T.; Guillot-Deudon, C.; Renaud, A.; Boujtita, M.; Jobic, S.; Lafond, A.; Influence of the Copper Deficiency and Anionic Composition on Band-Energy Diagram of Bulk Kesterite CZTSSe, *Mater. Res. Bull.* **2021**, *139*, 111285.

(24) Nguyen, T. K. N.; Dierre, B.; Grasset, F.; Renaud, A.; Cordier, S.; Lemoine, P.; Ohashi, N.; Uchikoshi, T.; Formation mechanism of transparent Mo_6 metal atom cluster film prepared by electrophoretic deposition, *J. Electrochem. Soc.* **2017**, *164*, D412.

(25) Guggenberger, L. J.; Sleight, A. W.; Structural and Bonding Characterizations of Molybdenum Dibromide, $Mo_6Br_{12}.2H_2O$, *Inorg. Chem.* **1969**, *8*, 2041.

(26) H. Schäfer, B. Plautz, H. Plautz, Die Dihydrate $[Me_6X_8^i]X_4^a.2H_2O$ mit Me = Mo, W; X = Cl, Br, J, *Z. anorg. allg. Chem.* **1971**, *389*, 57.

(27) Schoonover, J. R.; Zietlow, T. C.; Clark, D. L.; Heppert, J. A.; Chisholm, M. H.; Gray, H. B.; Sattelberger, A. P.; Woodruff, W. H.; Resonance Raman Spectra of $[M_6X_8Y_6]^{2-}$ Cluster Complexes (M = Mo, X; X, Y = Cl, Br, I), *Inorg. Chem.* **1996**, *35*, 6606-6613.

(28) Cordier, S.; Dorson, F.; Grasset, F.; Molard, Y.; Fabre, B.; Haneda, H.; Sasaki, T.; Mortier, M.; Ababou-Girard, S.; Perrin, C.; Novel Nanomaterials Based on Inorganic Molybdenum Octahedral Clusters, *J. Clus. Sci* **2009**, *20*, 9-21.

(29) Saito, N.; Cordier, S.; Lemoine, P.; Ohsawa, T.; Wada, Y.; Grasset, F.; Cross, J. S.; Ohashi, N.; Lattice and Valence Electronic Structures of Crystalline Octahedral Molybdenum Halide Clusters-Based Compounds, $Cs_2[Mo_6X_{14}]$ (X = Cl, Br, I), Studied by Density Functional Theory Calculations, *Inorg. Chem.* **2017**, *56*, 6234-6243.

(30) Baumann, H.; Plautz, H.; Schäfer, H.; Der Thermishe X^i/X^a-Austausch in $[Mo_6X^i_8]X^a_4$ (X = Cl, Br, I, OH), *J. Less-Common Metals* **1971**, *24*, 301-309.

(31) Marchuk, M. V.; Vorotnikova, N. A.; Vorotnikov, Y. A.; Kuratieva, N. V.; Stassb, D. V.; Shestopalov, M. A.; Optical Property Trends in a Family of $\{Mo_6I_8\}$ Aquahydroxo Complexes, *Dalton Trans.* **2021**, *50*, 8794-8802.

(32) Mikhaylov, M. A.; Abramov, P. A.; Komarov, V. Y.; Sokolov, M. N.; Cluster Aqua/Hydroxocomplexes Supporting Extended Hydrogen Bonding Networks. Preparation and Structure of a Unique Series of Cluster Hydrates $[Mo_6I_8(OH)_4(H_2O)_2]\bullet nH_2O$ (n = 2, 12, 14), *Polyhedron* **2017**, *122*, 241-246.

(33) Kepenekian, M.; Molard, Y.; Costuas, K.; Lemoine, P.; Gautier, R.; Ababou Girard, S.; Fabre, B.; Turban, P.; Cordier, S.; Red-NIR Luminescence of Mo_6 Monolayered Assembly Directly Anchored on Au(001), *Mater. Horiz.* **2019**, *6*, 1828-1833.

TOC

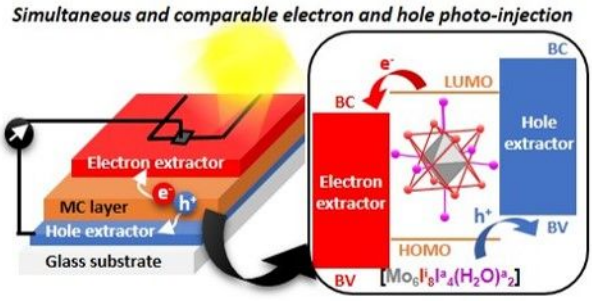
Simultaneous and comparable electron and hole photo-injection
Electron extractor
MC layer
Hole extractor
Glass substrate
BC
LUMO
Electron extractor
Hole extractor
HOMO
BV
BC
BV
[Mo6i8a4(H2O)a2]